This final draft may be downloaded for personal use only. Any other use requires prior permission of the American Society of Civil Engineers. This material may be found at https://doi.org/10.1061/(ASCE)EM.1943-7889.0001923

FINITE ELEMENT MODELING AND OPTIMIZATION OF 3D-PRINTED AUXETIC RE-ENTRANT STRUCTURES WITH STIFFNESS GRADIENT UNDER LOW-VELOCITY IMPACT

Florian Baertsch[1], Amir Ameli[2] and Thomas Mayer[3]

[1] Scientific Assistant, Institute of Mechanical Systems, School of Engineering, ZHAW - Zurich University of Applied Sciences, 8401 Winterthur, ZH, Switzerland.

[2] Assistant Professor, Plastics Engineering Department, University of Massachusetts Lowell, Lowell, MA 01854, USA (co-corresponding author). E-mail: amir_ameli@uml.edu

[3] Senior Lecturer, Institute of Mechanical Systems, School of Engineering, ZHAW - Zurich University of Applied Sciences, 8401 Winterthur, ZH, Switzerland (corresponding author). E-mail: thomas.mayer@zhaw.ch

ABSTRACT

Additive manufacturing technologies such as fused filament fabrication (FFF) allow the production of meta-structures with global properties that can be tailored to their specific application. This study aims to simulate and optimize an auxetic re-entrant structure with a stiffness gradient for enhanced energy absorption with low acceleration peaks under different low-velocity impact conditions. For this purpose, the finite element method (FEM) was used and appropriate constitutive models were fitted to static and dynamic tensile and compressive data of acrylonitrile butadiene styrene (ABS) tested under various strain rates. A Johnson Cook plasticity model demonstrated the best compromise between accuracy and computational efficiency. A simulation strategy using explicit FEM was further developed to simulate additively manufactured auxetic meta-structures under impact conditions. Good agreement was observed between the model prediction and the experimentally observed structural response. On this basis, a parametric optimization was implemented to enhance the energy absorption

capability with low acceleration peaks of a graded auxetic re-entrant structure for different impact velocities.

INTRODUCTION

Meta-structures can be designed to exhibit mechanical, electrical, acoustic, or thermal properties on a macroscopic level, that are different from those of the base materials. One of the mechanical properties that can be influenced by meta-structure design is Poisson's ratio, which describes the transverse deformation behavior of a material in response to longitudinal loading. Most natural materials have a positive Poisson's ratio, which is governed by their atomic packing density and crystal structure (Prawoto 2012); this means stretching in one direction leads to contraction in the transverse directions and vice versa.

Auxetic metamaterials have a negative Poisson's ratio, meaning that stretching in one direction leads to an expansion in the transverse directions. While made of conventional materials with positive Poisson's ratio, structural mechanisms such as hinging, bending, or stretching determine the overall macroscopic response that leads to a negative Poisson's ratio in auxetic metamaterials (Mir et al. 2014). Further advantages of auxetic metamaterials include their synclastic curvature property (D'Alessandro et al. 2018), that allows them to bend in the same direction on two perpendicular planes as well as their high indentation resistance (Evans and Alderson 2000). Auxetic metamaterials are anisotropic (Masters and Evans 1996) and exhibit lower stiffness, compared to their constituent material due to their cellular structure (Álvarez Elipe and Díaz Lantada 2012). The unconventional properties of auxetic metamaterials are beneficial for a variety of applications such as sports helmets with auxetic liner materials (Foster et al. 2018). Their favorable impact and energy absorption properties result in reduced impact accelerations. Other examples include civil engineering applications such as seismic metamaterials (Brûlé et al. 2020), biomedical applications (e.g., for blood vessels) (Aksu and Tather 2018) and sensing applications, making use of negative Poisson's ratios (Avellaneda and Swart 1998).

Favorable indentation and impact behavior for shock-absorber applications is reported specifically for auxetic re-entrant structures (Li et al. 2020), due to their high energy absorption performance and ability to reduce peak impact forces (Zhang et al. 2020). This is associated with their dynamic deformation mechanism in which the material is progressively drawn into the local loading zones as a result of their negative Poisson's ratio (Imbalzano et al. 2018; Qi et al. 2017; Yang et al. 2013). Experimental and numerical investigations (Zhou et al. 2017) have shown a three-stage force-displacement behavior of auxetic re-entrant structures under a uniaxial compression load. These stages are I) an elastic regime (elastic bending of the cell walls and the global lateral contraction due to the negative Poisson's ratio), II) a plateau regime (large deformation due to bending of vertical and inclined cell walls, plastic hinging, or local fracture), and III) a densification regime (frictional contact between the cell walls and compaction). Masters and Evans (1996) analytically modelled flexural, hinging, and stretching deformation modes in re-entrant structures to predict their basic anisotropic elastic properties from the unit cell dimensions as well as the cell wall angle and wall thickness. Fu et al. (2016) further showed that the in-plane shear moduli of re-entrant structures exhibit a nonlinear relation to the cell wall angle and the cell length-to-height ratio. Similarly, a strong dependence of the longitudinal and torsional stiffnesses on the cell wall angle was reported by Berinskii (2016). Dong et al. (2019) further performed an experimental and numerical study on the mechanical properties of metallic re-entrant honeycombs under quasi-static compressive loading. It was demonstrated that the deformation mechanism of the auxetic structure significantly depends on the wall thickness and the cell number. While thick-walled re-entrant structures tend to fracture locally and homogeneously contract towards the sample center, thin-walled structures were observed to contract locally and bulge out inhomogeneously on the sample boundaries. The plateau stress was found to be reasonably constant and independent of the negative Poisson's ratio, while, in the densification phase, the global force increase is significantly amplified by the negative Poisson's ratio due to increased transverse contraction that stiffens the compacted structure. In addition, it was shown that the energy absorption under quasi-static compression is dominated by plastic dissipation in both thick-walled and thin-walled structures, whereas a significant contribution of the elastic deformation energy is only observed for thin-walled structures. With increasing effective strain, the local fracture in thick-walled structures consumes up to 5% of the total dissipated energy.

In contrast to the quasi-static deformation behavior of auxetic re-entrant structures, their dynamic response is strain-rate dependent, firstly, due to the strain-rate sensitivity of the constituent material, and secondly, due to the inertia effects during dynamic loading (Zhang et al. 2020). The use of a more strain-rate sensitive base material generally leads to higher plateau stresses, whereas the inertia effect leads to the localization of crushing events at the loading ends which results in an enhanced dynamic strength for high loading speeds (Tan et al. 2005). While a more instable deformation behavior with global shear and lateral distortion is observed for quasi-static loading due to the buckling of the cell walls, dynamic loading is observed to be more homogeneous, featuring a layer wise collapse with negligible lateral distortion (Fíla et al. 2017). The dynamic deformation behavior is further reported to depend on the ductility of the base material. Brittle material tends to fracture locally leading to the simultaneous collapse of entire layers in auxetic re-entrant structures. In contrast, buckling-induced shear deformation is observed in ductile material (Zhang et al. 2020). Imperfections in additively manufactured structures further cause delamination during low-velocity impacts so that the energy absorption is reduced (Yazdani Sarvestani et al. 2018).

Sandwich structures with auxetic cores featuring re-entrant unit-cells are reported to be especially advantageous with respect to energy-absorption performance due to their layer wise failure behavior under impact loads. Thereby, transmitted impact loads are smaller in auxetic cores than in conventional hexagonal honeycomb cores during low-velocity impacts (Yazdani Sarvestani et al. 2018). In contrast to conventional honeycomb or foam cores that fail due to core shear, indentation, inter-laminar failure or face-sheet yield and wrinkle, auxetic cores adapt to outer loads by buckling-induced layer wise failure that helps to redistribute stress throughout the core and that enables bending of the global structure (Zhang et al. 2020). The energy absorption capacity is thus increased and the peak force is reduced for increasingly negative Poisson's ratios (Zhang et al. 2015).

Auxetic meta-structures can be manufactured at different length scales, from molecular structures up to microcellular foams and other larger cellular structures such as honeycombs and even larger scale structures (Evans and Alderson 2000). Generative fabrication methods such as additive manufacturing (AM) can print auxetic meta-structures with an increased level of complexity and minuscule features that are not achievable with conventional technologies so far (Zhang et al. 2020). Therefore, optimized and more efficient meta-structure designs can be tailored to a specific application to fully utilize the unconventional mechanical properties of auxetic meta-structures. A widely used type of polymer-based AM technique is fused filament fabrication (FFF). In FFF, the feedstock material, mostly a thermoplastic-based filament, is heated above its melting temperature and deposited on the build plate layer by layer until a complete part is generated (Aliheidari et al. 2017, 2018; Christ et al. 2017, 2018; Nadgorny and Ameli 2018). Acrylonitrile butadiene styrene (ABS) is a ductile thermoplastic filament material for general engineering applications.

Given the freedom to adapt the unit cell geometry (cell dimensions, length-to-height ratio, and cell wall angle and thickness) and the constituent material's characteristics (elastic modulus, yield stress, strain rate sensitivity, ductility, and manufacturing process), the metamaterial design can be tailored to the specific requirements of each application. To optimize its specific energy absorption capability for impact loads, auxetic re-entrant structures need to be designed such that as much kinetic energy as possible can be dissipated by plastic or viscoelastic deformation or friction. At the same time, peak forces need to be minimized for applications as impact protectors (Zhang et al. 2020). Novel design methods for auxetic metamaterials are still under development. These include experimental and heuristic approaches. For instance, Ren et al. (2018) developed an auxetic nail through experimental design variations and Wang et al. (2015) studied dual-material auxetic meta-structures experimentally and numerically. More recently, topology optimization techniques have been further developed to identify optimum auxetic unit cells. Zheng et al. (2020) used evolutionary topology optimization to establish orthotropic auxetic unit cells. Gao et al. (2020) proposed an isogeometric topology optimization approach to identify 2D and 3D re-entrant and chiral meta-structures. de Lima and Paulino (2019) applied topology optimization of compliant mechanisms including additive manufacturing constraints to design auxetic meta-structures. Typically, linear elastic material behavior is considered for these optimization approaches. Alternatively, parametric optimization varies geometrical parameters of an initially prescribed and parametrized unit cell. Thereby, non-linear material behavior can also be considered which is important to correctly predict the dissipated energy during impact loading. This nonlinear behavior is relevant due to the viscoelastic and plastic deformations as well as sliding friction and local failure. Wang et al. (2018) optimized a double-V auxetic structure made of a high-ductility stainless steel alloy using a non-linear constitutive model to improve its blast energy absorption capability. Beneficial energy absorption properties for a broader range of impact velocities have further been found by Cui et al. (2009) for foam materials featuring a stiffness gradient as implemented by a varying cell height within the meta-structure.

As the energy absorption capacity of cellular materials is significantly influenced by i) loading conditions (i.e., loading velocities that determine the deformation modes), ii) the unit cell geometry (i.e., the cell dimensions, length-to-height ratio, cell wall angle and thickness), and iii) the properties of their constituent materials (Zhang et al. 2020), the goal of this work is to perform a parametric optimization of an auxetic re-entrant structure to improve its energy absorption characteristic by reducing peak accelerations for low impact velocities of 2 and 5 m/s by introducing a stiffness gradient along the loading direction of the structure. For this study, the auxetic structures are manufactured by FFF using ABS material and non-linear, strain-rate dependent material properties are considered for the Finite Element (FE) simulations. Strategies are further presented to account for the manufacturing imperfections to more realistically predict both the dynamic structural response under low-strain rate and impact loading conditions using an explicit FE analysis. On this basis, a graded meta-structure is derived through parametric optimization with the goal of improving its acceleration profiles for two low-velocity impact scenarios.

EXPERIMENTAL PROCEDURE

3D Printing of Test Specimens and Re-Entrant Structures

Pure ABS pellets, grade MAGNUM 3404, were dried in a vacuum oven at 70° C for 18 hours under vacuum and subsequently extruded using a twin-screw extruder LTE16-40 (Lab Tech Engineering Company Ltd) with a die diameter of 1.75 [mm] and three heating zones (219, 256 and 217 [°C]). After extrusion, the filament was fan cooled, stretched to a diameter of 1.5 [mm] and wound onto a spool.

The fabricated ABS filament was used to print the tensile and compressive test specimens for material characterization as well as the auxetic re-entrant structures for the model validation. A custom made FFF printer and Simplify3D slicing software were used. The adopted printing parameters are listed in Table 1. The specimen geometries, dimensions, and print buildup directions are shown in Figure 1 for the tensile and compressive specimens.

To assess different deformation mechanisms, auxetic re-entrant structures with three different re-entrant angles, i.e. 30°, 45° and 70° were considered. Figure 2 shows the overall structure, dimensions, details, and print buildup direction of the respective samples. The number of layers and the cell width were kept constant so that the global height of the meta-structure varies with the re-entrant angles. An in-plane print buildup was used for the auxetic meta-structures to avoid the need for support structures. The same buildup direction was used for all the printed samples.

Mechanical Testing of Specimens and Re-Entrant Structures

Tensile and compressive tests were performed with low strain rates of 2.45×10^{-4} [-/s] to 1.32×10^{-2} [-/s]. The tensile tests were carried out according to ISO 527-2-1BA ("EN ISO 527-2: Determination of tensile properties of plastics" 2012). Compressive tests were conducted on cylindrical specimens with a diameter and a height of 20 [mm] each for material characterization purposes. The print buildup direction, cf. Figure 1a, was the same as the loading direction. Both experiments were performed on a Shimadzu AG-X Plus testing machine with a 20 [kN] load cell. Strains were measured by video-extensometry (LIMESS Messtechnik & Software GmbH). Tensile specimens were loaded until final failure, while compression specimens were loaded up to 19 [kN]. In total, ten tensile tests at four different strain rates and four compressive tests at two different strain rates were performed with at least two repetitions per condition. The FFF printed re-entrant meta-structures for model validation, cf. Figure 1b, were tested in compression under displacement control mode at a displacement rate of 5 [mm/min]. Depending on the re-entrant angle, this resulted in strain rates of 2.1×10^{-2} [-/s], 2.8×10^{-2} [-/s] or 4.3×10^{-2} [-/s]. Larger re-entrant angles resulted in larger heights of the structure and therefore lower strain rates. The tests were carried out with one sample per re-entrant angle.

MATERIAL CONSTITUTIVE MODEL

Figure 3a shows the tensile stress-strain behavior of the FFF printed ABS samples at different strain rates. The elongation at rupture decreases while the ultimate tensile strength increases with an increase in the strain rate. The modulus of elasticity does not exhibit a clear trend with strain rate and varies within ±30% in response to the tested strain rate range. This is presumably attributed to printing imperfections, as also pointed out in (Colón Quintana et al. 2019). Both print orientation and imperfections can lead to significant variations in the mechanical characteristics, which is not investigated further within the scope of this study. Figure 3b shows the compressive stress-strain behavior of FFF printed ABS for two different strain rates. The experimental data was smoothed using a moving average method as the delamination of axially loaded ligaments caused noise in the force signal. Both the stiffness and the viscoplastic plateau increased with an increase in the strain rate.

To cover both low strain rate and impact loading conditions within the FE models, a wide range of strain rates was considered for the constitutive modelling of the in-plane properties of FFF printed ABS. The experimental tensile and compressive data for strain rates of 1.5×10^{-4} [-/s] and 1.3×10^{-2} [-/s], and 2.4×10^{-4} [-/s], respectively, was therefore complemented with literature data of a high strain rate compressive test at 1.1×10^{4} [-/s] for conventionally produced ABS (Walley and Field 1994), cf. Figure 4. Furthermore, a Poisson's ratio of 0.36 for the base material was assumed for the constitutive models (Cantrell et al. 2017).

On the basis of the material data given in Figure 4, a set of conventional and more sophisticated constitutive models was calibrated using the commercial MCalibration software Version 5.1 by PolymerFEM LLC (Bergström 2015; PolymerFEM 2020). The parameters of any considered constitutive model were then optimized to minimize the normalized median absolute deviation (NMAD) between the model prediction and the experimental data of stress for a basic set of experiments (e.g. tensile and compression tests). The optimization algorithm used by the software was a Nelder-Mead downhill-simplex method. After calibration, the error was generally below 10% whereas the fit of the finally adopted Johnson-Cook model featured an error below 5%. The following material models were considered and compared:

- Elastic Plastic with Combined Hardening
- Johnson Cook Plasticity, with adaption for strain dependency (Bergström 2015)
- Parallel Rheological Framework Model (Bergström 2015)
- Three Network Viscoplastic Model (Bergström 2015).

These constitutive models were compared on the basis of virtual tensile tests with two strain rates (0.67 -/s and 6.7 -/s). For this purpose, a respective FE model was set up in Abaqus 2018 by Dassault Systems using both Abaqus internal implementations of the material models as well as user-defined material subroutines (UMAT) included in the PolyUMod® package of the

MCalibration software. An explicit solver was used for all the simulations in this study in order to efficiently cope with highly dynamic conditions as well as multiple self-contacts, as required for the final purpose of this study to simulate and optimize re-entrant auxetic structures under impact loads.

The simulated stress-strain behaviors for the considered material models are presented in Figure 5. As expected, the Elastic Plastic model with Combined Hardening was not able to represent any strain rate sensitivity while still being able to describe the softening behavior at larger strains. The Three Network Viscoplastic model and the Johnson Cook model showed similar behavior in terms of the ultimate tensile stresses and non-linear softening at different strain rates. The Parallel Rheological Framework model on the other hand exhibited a higher ultimate tensile stress at a relatively constant stress level for higher plastic strains.

The Johnson Cook model was finally selected for the subsequent modeling of the auxetic structures because of its qualitatively comparable behavior with respect to the more sophisticated Three Network Viscoplastic model and its general availability within the Abaqus framework that facilitates parallel computing.

MODELING OF AUXETIC STRUCTURES

To verify the material model performance and in order to be able to realistically simulate the global structural behavior of auxetic metamaterials, an FE model was set up based on a simple regular auxetic re-entrant structure as detailed in Figure 6a. Simulative predictions were compared with the experimental compression tests of the FFF printed structure. Figure 6balso shows the individual parameters used in the structure optimization study as further detailed in section *STRUCTURAL OPTIMIZATION OF STIFFNESS GRADIENT FOR IMPACT*.

Finite Element Modeling

Based on the parametrized geometry and the selected material model (Johnson Cook Plasticity model), an explicit structural simulation was set up in the FE software Abaqus to simulate both quasi-static displacement controlled compression (low-strain rate) and the dynamic impact load cases for the auxetic re-entrant structures. As shown in Figure 7a, the model was set up in 2D and the geometry was meshed with bilinear quadrilateral plane strain elements (CPE4R) with reduced integration and enhanced hourglass control. At least five elements were considered over the ligament thickness to appropriately cover bending, cf. Figure 7a. A coarser mesh, cf. Figure 7b, was later used in the simulation of impact for the parametric optimization of the stiffness gradient to reduce the computational effort from 4 hours per iteration to 20 min. As the acceleration profile was found to be predominantly influenced by the unit cell geometry and the constituent material, this simplification is justified for practical reasons. The optimized result was verified by a carefully conducted mesh study for the impact simulation showing that the basic deformation mechanism was not influenced by this mesh coarsening and that the maximum error in the predicted peak acceleration was less than 10%.

The boundary conditions implemented for the low-strain rate and dynamic impact load cases of the structural model are given in Figure 8a and 8b, respectively. All contacts were modeled as penalty contacts, with a friction coefficient of 0.3 (Baur et al. 2007). In order to optimize the computation time (13 to 370 s) of the low-strain rate compression load case, mass scaling was applied to reach a step size of 2×10^{-4} [s]. Further details on the specific changes for the dynamic impact simulation for the parametric optimization is given in *STRUCTURAL OPTIMIZATION OF STIFFNESS GRADIENT FOR IMPACT*.

Regular Re-Entrant Structure: Comparison of Simulation and Experiment

Figure 9 compares the global deformation characteristics of the experimental and simulated low strain rate compression tests of a regular auxetic re-entrant structure with 45° angle for six different strain levels. The auxetic behavior of the structure was apparent in both the experimental and simulated tests at low strain levels of less than 10% in the linear elastic regime. With the onset of the structural instability at higher compression levels (strain levels greater than ~10%), the initially localized instability became more global as whole layers crushed. Thereby, opposing faces of the horizontal cell walls came into contact, slid on top of each other and transmitted the load directly via a larger contact area. This lead to an increased stiffness with ongoing compression up to a point where the structure was fully compacted and a large share of internal faces was in contact turning the cellular structure to a quasi-dense material.

Figure 10 compares the experimentally measured global stress-strain behavior to the low-strain rate structural response predicted by the FE simulation for three different re-entrant structures. As seen in Figure 10, the experimental data and the simulation results are in good agreement in case of the structures with 30° and 45° re-entrant angles up to the densification phase of the simulation. More significant differences arise, however, for the flatter 70° re-entrant angle. In this case, the stress response was overestimated prior to the onset of the densification regime. While qualitatively coherent, quantitative discrepancies were observed in all structures during the densification phase.

The strong deviation in the predicted stress-strain behavior of the structure with 70° angle (Figure 10) can be explained by the assumption of a perfectly homogeneous material in the FE model that misses to account for the various imperfections contained in the real FFF printed structures. In addition to these material imperfections, geometrical imperfections are also not considered in the model. Figure 11 shows how stress builds up before the occurrence of the structural instability, i.e., sideward elastic-plastic buckling of the walls. In the model, the full load was transmitted via a mechanical form fit of the vertical cell walls that lead to an overestimation of the structural stiffness. In the actual structure, geometric imperfections prevent such a stiffening form fit, as a sideward sliding of the contacting surfaces is expected to occur, which reduces the resistance of the structure toward compression. As the compressive force was increased, slip was initiated in the model leading to a sudden reduction of the stress level and an increase in the strain as it is apparent in the predicted structural behavior, cf. Figure 10. This effect dominated the response of the structure with a re-entrant angle of 70° as its larger contact area promoted the occurrence of a form fit.

Further quantitative discrepancies in the densification phase may arise due to the local delamination damage in the joints as well as strong nonlinearities resulting from the friction dominated deformation behavior. Delamination was not accounted for in the FE model and the accurate prediction of nonlinear friction in multiple contact areas was impeded by the rough and imperfect surfaces of the FFF printed structures.

Enhanced Model of Re-Entrant Structure

As demonstrated in Figure 12a and 12b, the FFF printed auxetic structures with larger re-entrant angles (45° and 70°) exhibit larger inner radii than their nominal values used in the FE models. Image analysis of the actual printed structures using ImageJ software revealed mean values of the radius (as identified by a red circle 2 in Figure 12a) of 0.31 [mm] and 0.20 [mm] for the 70° and 45° structures, respectively, instead of the specified nominal values of 0.15 [mm]. The initial FE model thus deviated significantly from the real dimensions in the case of the 70° structure. An enhanced FE model was thus setup using the actual radii of the as-printed structures.

Moreover, some geometrical imperfections were observed in the joint regions, especially in the printed structures with a 70° re-entrant angle, as identified by circle 1) in Figure 12a. The actual misalignment presumably led to an earlier onset of sideward slippage in the experiment, and thus to a more compliant structure, as a consequent of the absence of a force build-up due to the form fit. To facilitate the onset of inherent instabilities in the presence of such defects, local perturbations were introduced to the enhanced FE model by small force couples (4 N each) as indicated in Figure 12b with the red arrows. The force couples were implemented as concentrated forces on reference points that were coupled to all of the incident corners of the re-entrant structure. They were activated only temporarily over an estimated time period required for the incident corners of the re-entrant structure to establish their contact. It is noted that the structure was kept in equilibrium, i.e. the global resulting force and moment due to the perturbation were zero. Locally, however, earlier sideward slippage of the contacting faces was initiated so that the elastic-plastic buckling of the cell walls could occur prior to the formation of a form fit with the associated stiffening of the structure. This approach is especially practical, as the deformation behavior can be modelled more realistically without having to implement the actual geometrical imperfections of the printed structure.

The radius corrections for the structures with 70° and 45° re-entrant angles and the introduction of a perturbation to the 70° structure leads to a significant improvement in the model predictions and better agreement with the experimental results during the instability phase, cf. Figure 10 (initial model) and Figure 13 (enhanced model). To account for the delamination effects and to further improve the predictions at the densification regime, a damage model needs to be implemented in future work.

STRUCTURAL OPTIMIZATION OF STIFFNESS GRADIENT FOR IMPACT

Structural Optimization Model

Energy absorbent structures need to convert kinetic energy into elastic, viscoelastic, and plastic deformation or dissipate energy as heat (frictional deformation, fracture / delamination) effectively at a range of impact velocities while keeping the acceleration peaks as low as possible. Appropriately designed stiffness gradients in impact direction can mitigate the consequences of an impact more effectively for a wider range of velocities as volumes of varying stiffnesses react differently to different impact energies (Cui et al. 2009).

With the goal to improve the energy absorption characteristic of an auxetic re-entrant structure by minimizing the peak accelerations that occur for low-velocity impacts, a parametric optimization was set up. The structure was then optimized for two equivalently prioritized impact scenarios involving an impacting mass of 0.4 [kg] with the velocities of 2 [m/s] and 5 [m/s], which were equivalent to kinetic impact energies of 0.5 [J/mm] and 5 [J/mm], respectively. An attenuation of acceleration peaks was to be accomplished by implementing a stiffness gradient along the impact direction.

To realize a stiffness gradient, the geometry of an auxetic re-entrant structure with four layers and variable height was parametrized by five geometrical parameters, cf. Figure 6b, as listed below:

- layer height difference x that determines the unit cell height gradient according to $h_1 = h_2 + x = h_3 + 2x = h_3 + 3x$ (with h_i being the height of layer $i = 1$ to 4)
- contact distance y, i.e., the minimum vertical distance between the layers, which was kept constant for each layer
- inner radius of the incident corners, which determines the rotational stiffness of the inclined walls
- width of the unit cell, which was kept constant at 5 [mm]
- wall thickness of the unit cell, which was kept constant at 0.5 [mm])

A preliminary sensitivity analysis revealed significant dependencies of the peak accelerations on the layer height difference x and the contact distance y, which together result in a variation of the cell wall angle over the height of the re-entrant structure. Furthermore, the inner radius appears to have a minor effect on the peak acceleration. In order to reduce the geometric parameters for the optimization, the inner radius was set to 0.2 [mm], the wall thickness was set 0.5 [mm] and the width of the unit cell was kept constant at 0.5 [mm]. So, finally, two parameters were considered for the structural optimization: 1) the layer height difference x, and 2) the contact distance y.

Thus, the optimization problem aimed to minimize an objective function as in Eq. (1) that is subject to constraints of (2) – (7). The objective function was the weighted sum of the peak accelerations that result from the impacts with 5 and 2 [m/s], i.e., $a_5(x, y)$ and $a_2(x, y)$, respectively. To ensure equal consideration of both impact velocities in the optimized solution, a weighting factor of $w = 6.25$ [-] was implemented that corresponds to the ratio of the kinetic energies of the respective impact scenarios. Additionally, the peak accelerations were limited to greater than 1000 [mm/s^2], i.e., constraints (2) and (3), in order to prevent the optimization toward invalid parameter sets, and the two geometric parameters need to be within the range $x = $ [1 mm, 2mm] and $y = $ [0.5 mm, 2mm], i.e. constraints (4) to (7).

$$\min \{a_5(x,y) + w * a_2(x,y): x,y \epsilon \mathbb{R}\} \tag{1}$$

$$1000 \leq a_5(x,y) \tag{2}$$

$$1000 \leq a_2(x,y) \tag{3}$$

$$x_{min} \leq x \tag{4}$$

$$y_{min} \leq y \tag{5}$$

$$x \leq x_{\max} \tag{6}$$

$$y \leq y_{\max} \tag{7}$$

The optimization was set up in SIMULIA Isight. In order to ensure both an effective global search for an optimum design point as well as an efficient local optimization, a combination of an Evolutionary and a Hooke-Jeeves algorithm was applied. The design space was initially explored via the Evolutionary algorithm to find local minima. These intermediate results were subsequently optimized using a focused local search using the Hooke-Jeeves algorithm. The optimization interrupted when no significant change of the objective function was detected upon unit change of the parameters.

Modeling of Structures under Impact

The finite element model was set up in Abaqus Explicit, analogous to the model used for the low-strain rate compression testing of the regular auxetic re-entrant structure as described above. As shown in Figure 8b, the impact loading was applied by impacting a planar rigid body surface with prescribed initial velocity according to the two impact scenarios, i.e., 5 [m/s] and 2 [m/s], and given an effective mass of 0.4 [kg/mm] per unit thickness of the meta-structure, i.e. 15 [mm].

As described in section *Finite Element Modeling,* the expected high number of iterations in the parametric optimization implies the use of a coarser mesh in order to reduce the computation times. The mesh size influences the computation time in two ways: 1) through the number of degrees of freedom of the system; and 2) through the shock wave traveling time within an element influencing the applicable time increments in explicit simulations.

Carefully conducted mesh sensitivity studies implied that the number of elements over the wall thickness can be reduced from 5 to 2 elements, cf. Figure 7b, without significant loss of accuracy (less than 10% deviation in the predicted peak accelerations) and without affecting the deformation modes. Thereby, the number of degrees of freedom is reduced significantly so that the calculation times can be brought down by a factor of 12. Subsequent to the optimization with the coarse mesh, a verification of the optimized solution was also performed using a fine mesh to confirm the reduced peak acceleration.

In order to reduce the number of increments that need to be solved for a load case, the applicable time increments need to be increased for explicit simulations. For this purpose, the shock wave traveling time within an element needs to be increased by mass scaling. The addition of an artificial lumped mass in an element thereby increases the shock wave travelling time and therefore the applicable time increments of the explicit simulation. Care must be taken to assure that the dynamic structural response is not affected by the addition of the lumped mass. To verify the validity of the approach, a sensitivity study was performed to check the artificial mass for the coarse mesh. As a result, a reasonable compromise between the accuracy and the computation time was found for a mass scaling with 0.078 % of the added mass allowing for maximum time increments of 10^{-7} [s], cf. Figure 14. While further addition of mass lead to longer applicable time increments of 5×10^{-7} [s], the resulting errors of the predicted peak accelerations were around 25 % and therefore not acceptable.

Both the use of a coarse mesh and the utilization of a mass scaling are justified for practical reasons to speed up the optimization process. As the geometrical parameters are expected to dominate the resulting peak accelerations, the effect of these simplifications are judged to be negligible.

Optimization Results

The global optimization using the Evolutionary algorithm did not show a clear trend towards a distinct optimum solution indicating that the optimization problem was ill-conditioned, i.e. the constrained objective function was not smooth and multiple local minima existed. Therefore, several local optima were identified and further optimized using the Hooke-Jeeves algorithm. Table 2 summarizes the baseline, initial and optimized parameters of the best local optimization.

Figure 15 compares the acceleration profiles of the two impact scenarios for the optimized and the regular (baseline) auxetic re-entrant structure as simulated using a fine mesh. The optimized re-entrant structure with stiffness gradient reduced the acceleration peak for impacts with 2 [m/s] by 46 %, while it increased the peak by 28 % in the case of the faster impacts with 5 [m/s] with respect to the baseline geometry. This change of the structural response can be explained by the height gradient of the different layers, resulting in the targeted stiffness gradient (Cui et al. 2009).

Figure 16 and Figure 17 compare the deformation behavior of a) the optimized re-entrant structure with stiffness gradient with b) the regular re-entrant structure (baseline) for impacts with 2 [m/s] and 5 [m/s], respectively. For the low impact velocity of 2 [m/s], the stiffness gradient caused a defined gradual layer wise collapse of the structure from top (larger cell heights) to bottom (smaller cell heights) whereas the bottom layer did not appear to collapse fully, cf. Figure 16a. In contrast, the collapse of the layers in the structure without stiffness gradients was rather randomly localized but still uniform, cf. Figure 16b. For the higher impact velocity 5 [m/s], the layer wise deformation in the early stage of the impact was not only confined to the top layer but further layers with smaller cell heights were already affected, cf. Figure 17 a). Thereby, a more homogeneous compaction through collapse and compaction of all layers was observed at earlier stages, compared to the case of the lower impact velocity. The regular re-entrant structure, in contrast, exhibited stronger localization and collapse of all layers at an early stage whereas the optimized structure still featured an intact elastically deforming layer at the bottom. This indicates that the implementation of a stiffness gradient can be used to better accommodate for wider impact ranges. The optimization of the layer height difference and distance between layers presented here, resulted in an improved design for slower impacts. A shift to better absorb impacts of higher velocities can be realized by decreasing the weight factor in the objective function (1), thereby prioritizing higher velocity impacts.

The acceleration response of a mass impacting the optimized structure at various velocities is shown in Figure 18**.** The peak accelerations for 1, 2 and 3 m/s are comparable, while the impacts with 4 and 5 m/s lead to excessive accelerations. This indicates that the optimized structure presented here reaches its limits for these cases as it is fully compressed and exhibiting excessively stiff mechanical behavior during these impact situations, as also seen in Figure 17a. This is a consequence of the full compaction of the structure such that it behaves comparatively stiff and similar to a bulk material. To improve the design of this graded structure, additional layers, e.g., with thicker walls or a layer of a stiffer foam could be included to improve the absorption behavior for higher kinetic energies.

CONCLUSION

A dynamic explicit FE model was established for the simulation of auxetic re-entrant structures under low-velocity impact conditions. For this purpose, different constitutive models were calibrated and compared for a range of strain rates. A Johnson-Cook type model was found to effectively represent the material characteristics while featuring decisive computational advantages. Good agreement was obtained between the simulated and experimental stress values for the compressive deformation characteristics of auxetic re-entrant structures with different angles in the elastic and instability phases of the response. Deviations in the densification phase of the deformation were attributed to delamination processes that are not accounted for in the model. Further improvement of the FE model was achieved for higher re-entrant angles by considering the printing imperfections via correction of the inner radii, and by accounting for the geometrical imperfections through local perturbations that allow for an earlier onset of buckling in the instability phase.

The established dynamic explicit simulation allowed the modeling of low velocity impacts and strain rate dependent deformation behavior. This simulation was used for a parametric optimization of an auxetic re-entrant structure with stiffness gradient with the goal to minimize peak accelerations during two low velocity impact scenarios. The results of the parametric optimization showed that a stiffness gradient enhances the energy absorption performance of meta-structures with auxetic properties at different impact velocities. Computationally optimized simulation models in combination with appropriate optimization algorithms have a large potential as automatized tools for the simulation driven design of mechanical and physical properties of metamaterials.

DATA AVAILABILITY STATEMENT

All data, models, or code that support the findings of this study are available from the corresponding author upon reasonable request.

ACKNOWLEDGEMENTS

This study was conducted in the course of an exchange program between Washington State University (WSU) and Zurich University of Applied Sciences (ZHAW) with support of a scholarship by the Hirschmann Foundation which is gratefully acknowledged. Special thanks are further due to Prof. Dr. Robert Eberlein and Matthias Huber for their support in testing and material modeling as well as to Ralf Pfrommer for helpful discussions concerning explicit modeling.

REFERENCES

Aksu, U., and Tather, S. (2018). “an Investigation on Recent Trends in Metamaterial Types and

Its Applications.” *i-manager's Journal on Material Science*, 5(4), 55.

Aliheidari, N., Christ, J., Tripuraneni, R., Nadimpalli, S., and Ameli, A. (2018). “Interlayer adhesion and fracture resistance of polymers printed through melt extrusion additive manufacturing process.” *Materials and Design*, Elsevier Ltd, 156, 351–361.

Aliheidari, N., Tripuraneni, R., Ameli, A., and Nadimpalli, S. (2017). “Fracture resistance measurement of fused deposition modeling 3D printed polymers.” *Polymer Testing*, 60, 94–101.

Álvarez Elipe, J. C., and Díaz Lantada, A. (2012). “Comparative study of auxetic geometries by means of computer-aided design and engineering.” *Smart Materials and Structures*, 21(10).

Avellaneda, M., and Swart, P. J. (1998). “Calculating the performance of 1–3 piezoelectric composites for hydrophone applications: An effective medium approach.” *The Journal of the Acoustical Society of America*, 103(3), 1449–1467.

Baur, E., Brinkmann, S., Osswald, T. A., and Schmachtenberg, E. (2007). “Kunststoffe im Vergleich.” *Saechtling Kunststoff Taschenbuch*, 746–747.

Bergström, J. (2015). *Mechanics of Solid Polymers*. Elsevier.

Berinskii, I. E. (2016). “Elastic networks to model auxetic properties of cellular materials.” *International Journal of Mechanical Sciences*, Elsevier, 115–116, 481–488.

Brûlé, S., Enoch, S., and Guenneau, S. (2020). “Emergence of seismic metamaterials: Current state and future perspectives.” *Physics Letters, Section A: General, Atomic and Solid State Physics*, Elsevier B.V., 384(1), 126034.

Cantrell, J., Rohde, S., Damiani, D., Gurnani, R., Di Sandro, L., Anton, J., Young, A., Jerez, A., Steinbach, D., Kroese, C., and Ifju, P. (2017). “Experimental characterization of the mechanical properties of 3D printed ABS and polycarbonate parts.” *Conference Proceedings of the Society for Experimental Mechanics Series*, 3, 89–105.

Christ, J. F., Aliheidari, N., Ameli, A., and Pötschke, P. (2017). “3D printed highly elastic strain sensors of multiwalled carbon nanotube/thermoplastic polyurethane nanocomposites." *Materials & Design*, 131, 394–401.

Christ, J. F., Aliheidari, N., Pötschke, P., and Ameli, A. (2018). "Bidirectional and stretchable piezoresistive sensors enabled by multimaterial 3D printing of carbon nanotube/thermoplastic polyurethane nanocomposites." *Polymers*, 11(1).

Colón Quintana, J. L., Heckner, T., Chrupala, A., Pollock, J., Goris, S., and Osswald, T. (2019). "Experimental study of particle migration in polymer processing." *Polymer Composites*, 40(6), 2165–2177.

Cui, L., Kiernan, S., and Gilchrist, M. D. (2009). "Designing the energy absorption capacity of functionally graded foam materials." *Materials Science and Engineering A*, 507(1–2), 215–225.

D'Alessandro, L., Zega, V., Ardito, R., and Corigliano, A. (2018). "3D auxetic single material periodic structure with ultra-wide tunable bandgap." *Scientific Reports*, 8(1), 1–9.

Dong, Z., Li, Y., Zhao, T., Wu, W., Xiao, D., and Liang, J. (2019). "Experimental and numerical studies on the compressive mechanical properties of the metallic auxetic reentrant honeycomb." *Materials and Design*, The Authors, 182, 108036.

"EN ISO 527-2: Determination of tensile properties of plastics." (2012). *Determination of tensile properties of plastics*, DIN EN ISO 527-2.

Evans, K. E., and Alderson, A. (2000). "Auxetic materials: Functional materials and structures from lateral thinking!" *Advanced Materials*, 12(9), 617–628.

Fíla, T., Zlámal, P., Jiroušek, O., Falta, J., Koudelka, P., Kytýř, D., Doktor, T., and Valach, J. (2017). "Impact Testing of Polymer-filled Auxetics Using Split Hopkinson Pressure Bar." *Advanced Engineering Materials*, 19(10), 1–13.

Foster, L., Peketi, P., Allen, T., Senior, T., Duncan, O., and Alderson, A. (2018). "Application of Auxetic Foam in Sports Helmets." *Applied Sciences*, 8(3), 354.

Fu, M. H., Xu, O. T., Hu, L. L., and Yu, T. X. (2016). "Nonlinear shear modulus of re-entrant hexagonal honeycombs under large deformation." *International Journal of Solids and Structures*, 80, 284–296.

Gao, J., Xiao, M., Gao, L., Yan, J., and Yan, W. (2020). "Isogeometric topology optimization for computational design of re-entrant and chiral auxetic composites." *Computer Methods in Applied Mechanics and Engineering*, Elsevier B.V., 362, 112876.

Imbalzano, G., Linforth, S., Ngo, T. D., Lee, P. V. S., and Tran, P. (2018). "Blast resistance of auxetic and honeycomb sandwich panels: Comparisons and parametric designs." *Composite Structures*, Elsevier Ltd, 183(1), 242–261.

Li, T., Liu, F., and Wang, L. (2020). "Enhancing indentation and impact resistance in auxetic composite materials." *Composites Part B: Engineering*, 198, 108229.

de Lima, C. R., and Paulino, G. H. (2019). "Auxetic structure design using compliant mechanisms: A topology optimization approach with polygonal finite elements." *Advances in Engineering Software*, Elsevier, 129(May 2018), 69–80.

Masters, I. G., and Evans, K. E. (1996). "Models for the elastic deformation of honeycombs." *Composite Structures*, 35(4), 403–422.

Mir, M., Ali, M. N., Sami, J., and Ansari, U. (2014). "Review of mechanics and applications of auxetic structures." *Advances in Materials Science and Engineering*, 2014, 1–18.

Nadgorny, M., and Ameli, A. (2018). "Functional Polymers and Nanocomposites for 3D Printing of Smart Structures and Devices." *ACS Applied Materials and Interfaces*, review-article, American Chemical Society, 10(21), 17489–17507.

PolymerFEM. (2020). "PolymerFEM." <https://polymerfem.com/introduction-to-mcalibration/> (Oct. 31, 2020).

Prawoto, Y. (2012). "Seeing auxetic materials from the mechanics point of view: A structural review on the negative Poisson's ratio." *Computational Materials Science*, Elsevier B.V., 58(August), 140–153.

Qi, C., Remennikov, A., Pei, L. Z., Yang, S., Yu, Z. H., and Ngo, T. D. (2017). "Impact and close-in blast response of auxetic honeycomb-cored sandwich panels: Experimental tests and numerical simulations." *Composite Structures*, Elsevier Ltd, 180, 161–178.

Ren, X., Shen, J., Tran, P., Ngo, T. D., and Xie, Y. M. (2018). "Auxetic nail: Design and experimental study." *Composite Structures*, 184(September 2017), 288–298.

Tan, P. J., Reid, S. R., Harrigan, J. J., Zou, Z., and Li, S. (2005). "Dynamic compressive strength properties of aluminium foams. Part i - Experimental data and observations." *Journal of the Mechanics and Physics of Solids*, 53(10), 2174–2205.

Walley and Field. (1994). "Strain rate sensitivity of polymers in compression from low to high rates." (January 1994).

Wang, K., Chang, Y. H., Chen, Y. W., Zhang, C., and Wang, B. (2015). "Designable dual-material auxetic metamaterials using three-dimensional printing." *Materials and Design*, Elsevier Ltd, 67, 159–164.

Wang, Y., Zhao, W., Zhou, G., and Wang, C. (2018). "Analysis and parametric optimization of a novel sandwich panel with double-V auxetic structure core under air blast loading." *International Journal of Mechanical Sciences*, Elsevier Ltd, 142–143(May), 245–254.

Yang, S., Qi, C., Wang, D., Gao, R., Hu, H., and Shu, J. (2013). "A comparative study of ballistic resistance of sandwich panels with aluminum foam and auxetic honeycomb cores." *Advances in Mechanical Engineering*, 2013.

Yazdani Sarvestani, H., Akbarzadeh, A. H., Niknam, H., and Hermenean, K. (2018). "3D printed architected polymeric sandwich panels: Energy absorption and structural performance." *Composite Structures*, Elsevier, 200(March), 886–909.

Zhang, J., Lu, G., and You, Z. (2020). "Large deformation and energy absorption of additively manufactured auxetic materials and structures: A review." *Composites Part B: Engineering*, Elsevier Ltd, 201(April), 108340.

Zhang, X. C., Ding, H. M., An, L. Q., and Wang, X. L. (2015). "Numerical investigation on dynamic crushing behavior of auxetic honeycombs with various cell-wall angles."

Advances in Mechanical Engineering, 7(2).

Zheng, Y., Wang, Y., Lu, X., Liao, Z., and Qu, J. (2020). "Evolutionary topology optimization for mechanical metamaterials with auxetic property." *International Journal of Mechanical Sciences*, Elsevier Ltd, 179(February).

Zhou, Z., Zhou, J., and Fan, H. (2017). "Plastic analyses of thin-walled steel honeycombs with re-entrant deformation style." *Materials Science and Engineering A*, Elsevier B.V., 688(January), 123–133.

CAPTIONS

Figure 1. Technical drawing of a) dog bone specimen for tensile test according to EN ISO5272 and b) cylindrical specimen for compressive test.

Figure 2. Technical drawing of the auxetic re-entrant structure with an inner angle of 45°.

Figure 3. Representative stress-strain response of printed ABS samples loaded at different strain rates: a) tensile loading and b) compressive loading (stresses and strains as absolute values).

Figure 4. The data set used in the calibration of the material constitutive models.

Figure 5. Comparison of the various calibrated constitutive models at two different strain rates.

Figure 6. a) Simple regular auxetic re-entrant samples for quasi static model verification (variable angle marked in red) and b) auxetic re-entrant geometry used for the optimization of stiffness gradient, with the individual optimization parameters.

Figure 7. Mesh of one unit cell for a) the quasi static model (geometry with an angle of 30°) and b) the dynamic model for the stiffness gradient optimization.

Figure 8. Sketch of the applied boundary conditions for a) the quasi static displacement-controlled loading and b) the dynamic loading.

Figure 9. Comparison of the a) experimental and b) simulated compression test results of the simple regular auxetic re-entrant structure with 45° angle at six different strain levels.

Figure 10. Comparison of the stress-strain behavior obtained from the regular finite element prediction and the experimental compression tests for the structures with three different re-entrant angles.

Figure 11. FE model of the structure with an angle of 70° at a strain of 15%. The von Mises stress contours show an increase in the stress due to a form fit creating a direct load paths at the onset of contact.

Figure 12. a) Visible imperfections (circle 1) and 2)) and bigger radii (circle 2)) of the printed 70° structure and (b) force couples introduced to the FE model to induce early instability.

Figure 13. Comparison of the stress-strain behaviors obtained from the enhanced finite element prediction and the experimental compression tests for the structures with three different re-entrant angles.

Figure 14. The effect of three different time steps on the acceleration profiles of the re-entrant structures with incorporated mass scaling to reduce computation time.

Figure 15. Comparison of the optimized structure to the baseline accelerations under 5 m/s and 2 m/s impact velocity.

Figure 16. Simulated impact at 2 m/s on a) optimized and b) baseline re-entrant structure.

Figure 17. Simulated impact at 5 m/s on a) optimized and b) baseline re-entrant structure.

Figure 18. Plot of reaction accelerations under various impact velocities.

TABLES

Table 1. FFF parameters used for the 3D printing of ABS.

Parameter	Value
Filament diameter [mm]	1.5
Print nozzle diameter [mm]	0.25
Nozzle temperature [ºC]	255
Bed temperature [ºC]	95
Layer height [mm]	0.2
Line width [mm]	0.3
Print Speed [mm/s]	55

Table 2. Comparison of baseline, initial and optimized parameters of the auxetic re-entrant structure with stiffness gradient.

Parameter	Baseline	Initial	Optimized
Layer height difference x [mm]	0	1.5	1.1
Contact distance y [mm]	0.5	1.915	1.567

a)

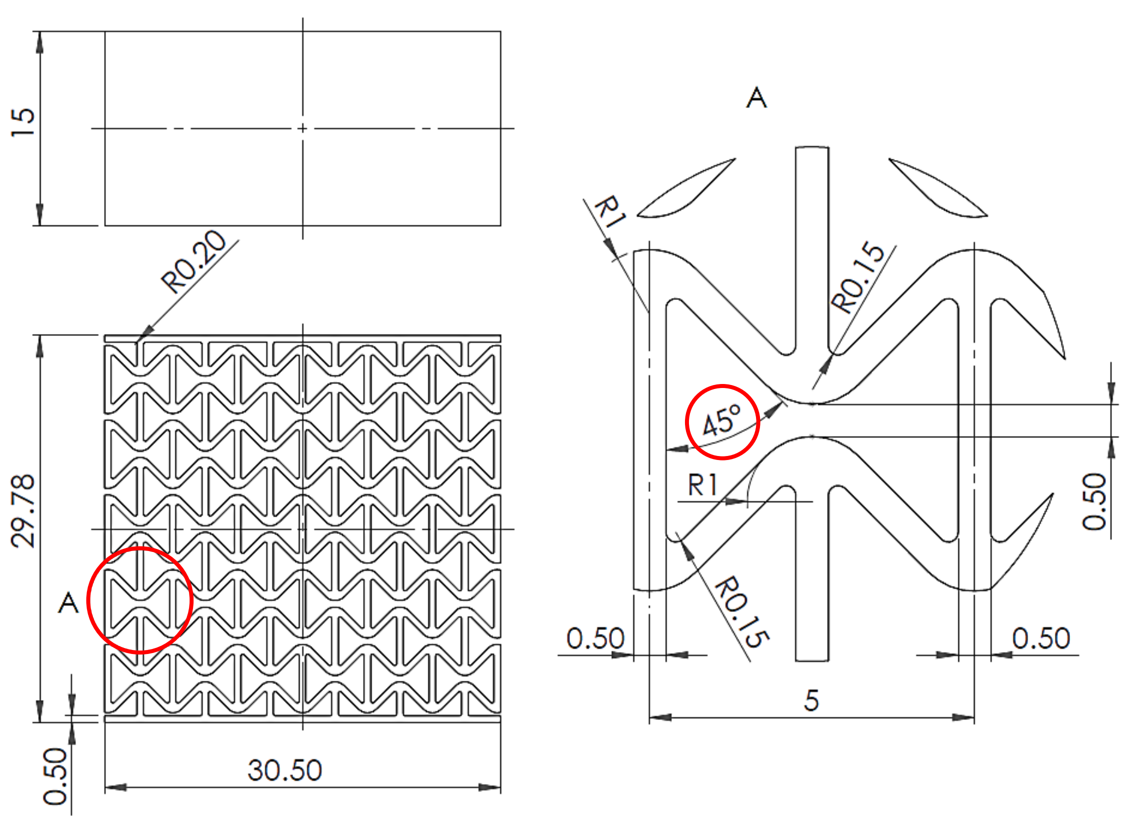
15
R0.20
29.78
A
0.50
30.50
A
R1
R0.15
45°
R1
R0.15
0.50
0.50
5
0.50

b)

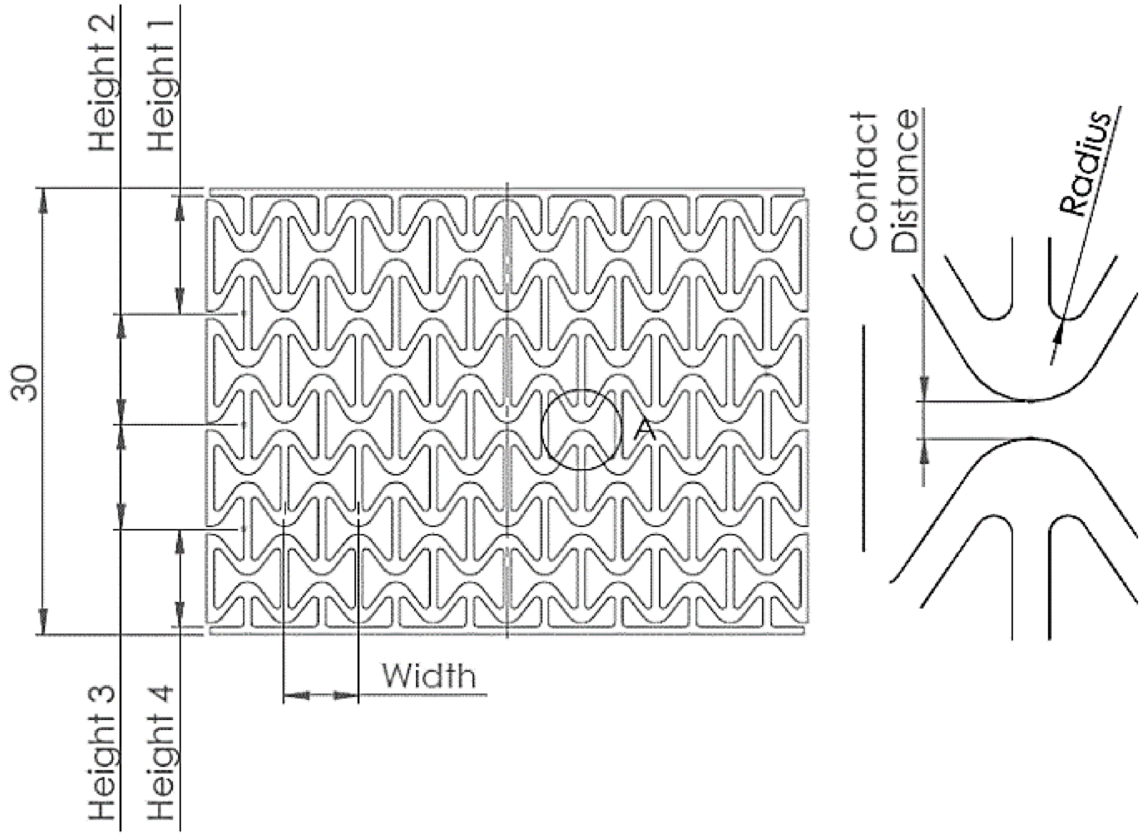
Height 2
Height 1
30
A
Width
Height 3
Height 4
Contact
Distance
Radius

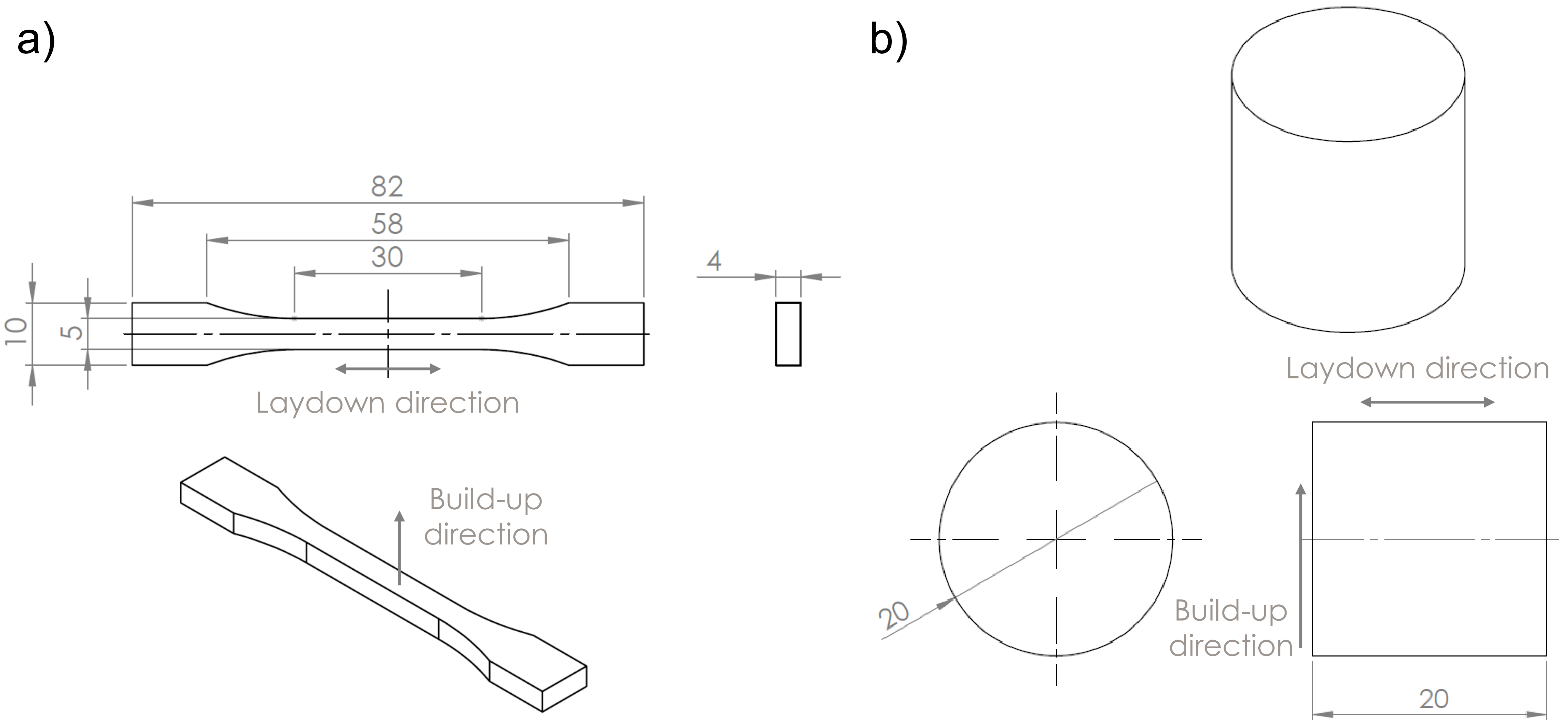
a)
82
58
30
10
5
4
Laydown direction
Build-up
direction
b)
Laydown direction
20
Build-up
direction
20

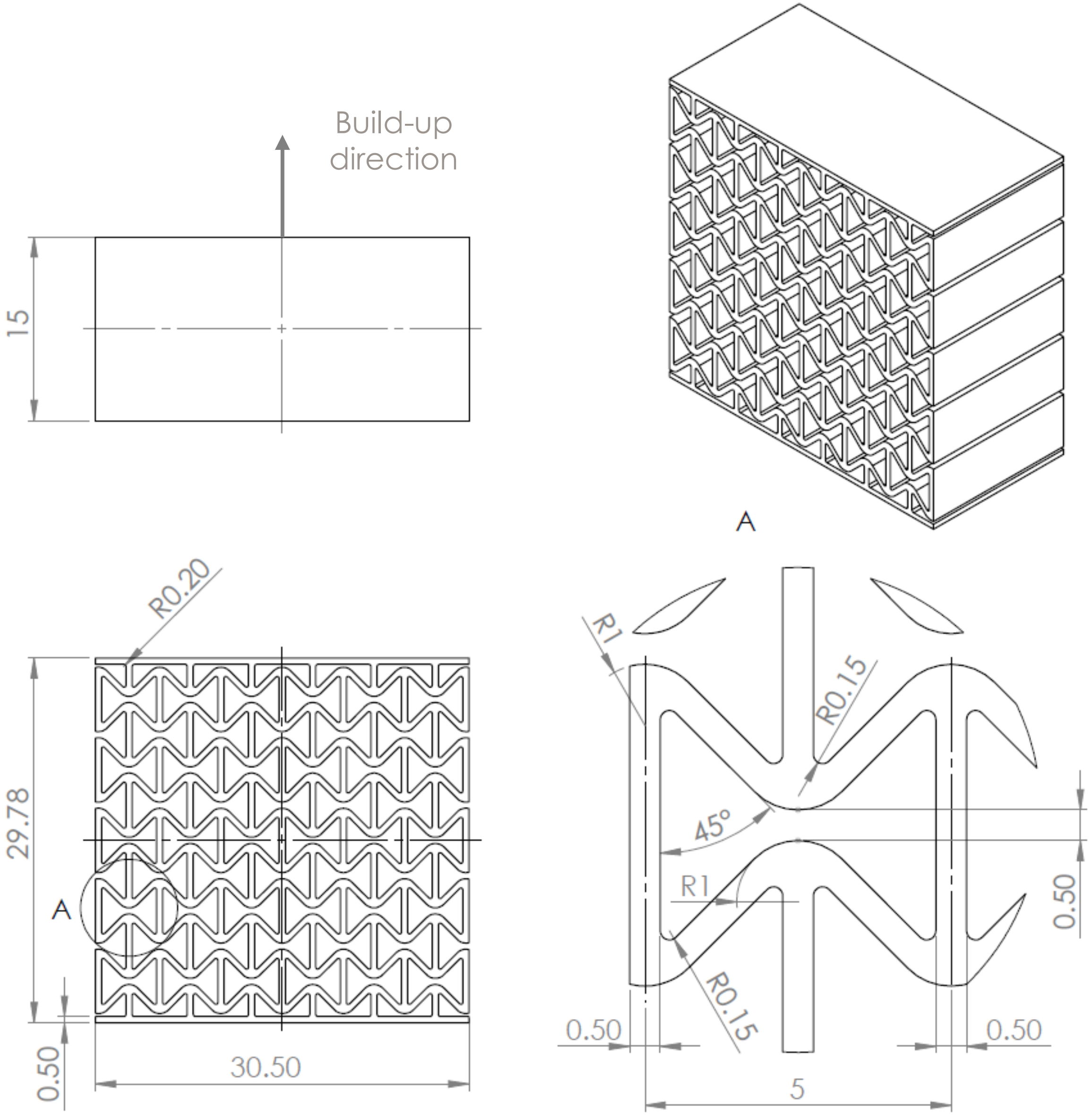
Build-up
direction
15
R0.20
29.78
A
0.50
30.50
A
R1
R0.15
45°
R1
0.50
R0.15
0.50
0.50
5

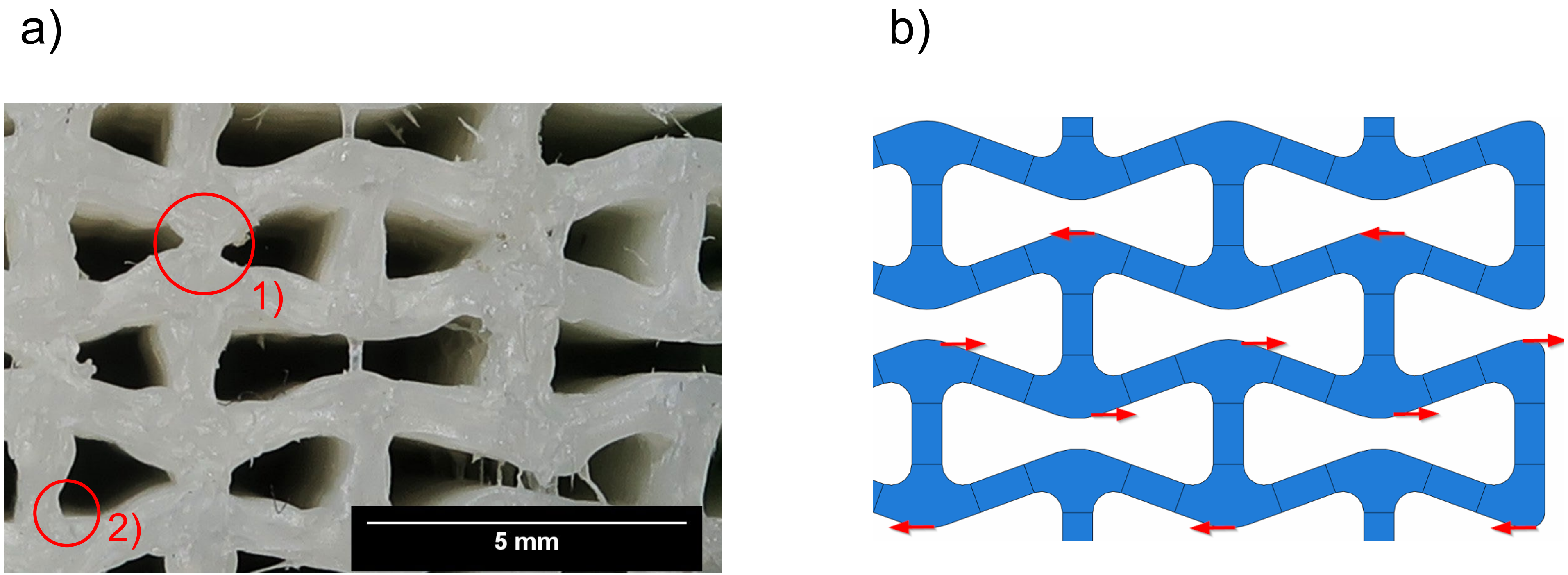
a)
b)
1)
2)
5 mm

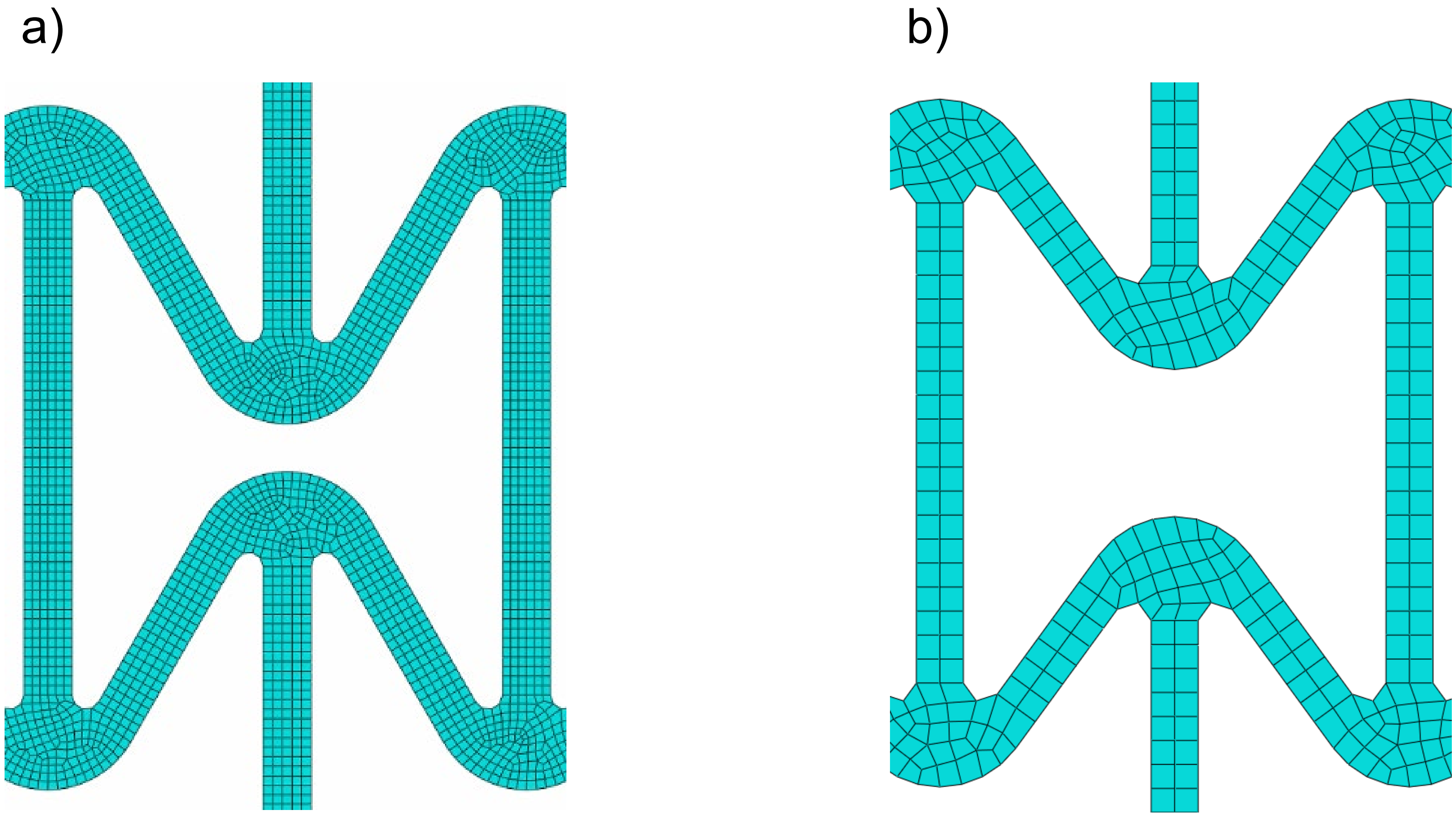
a)
b)

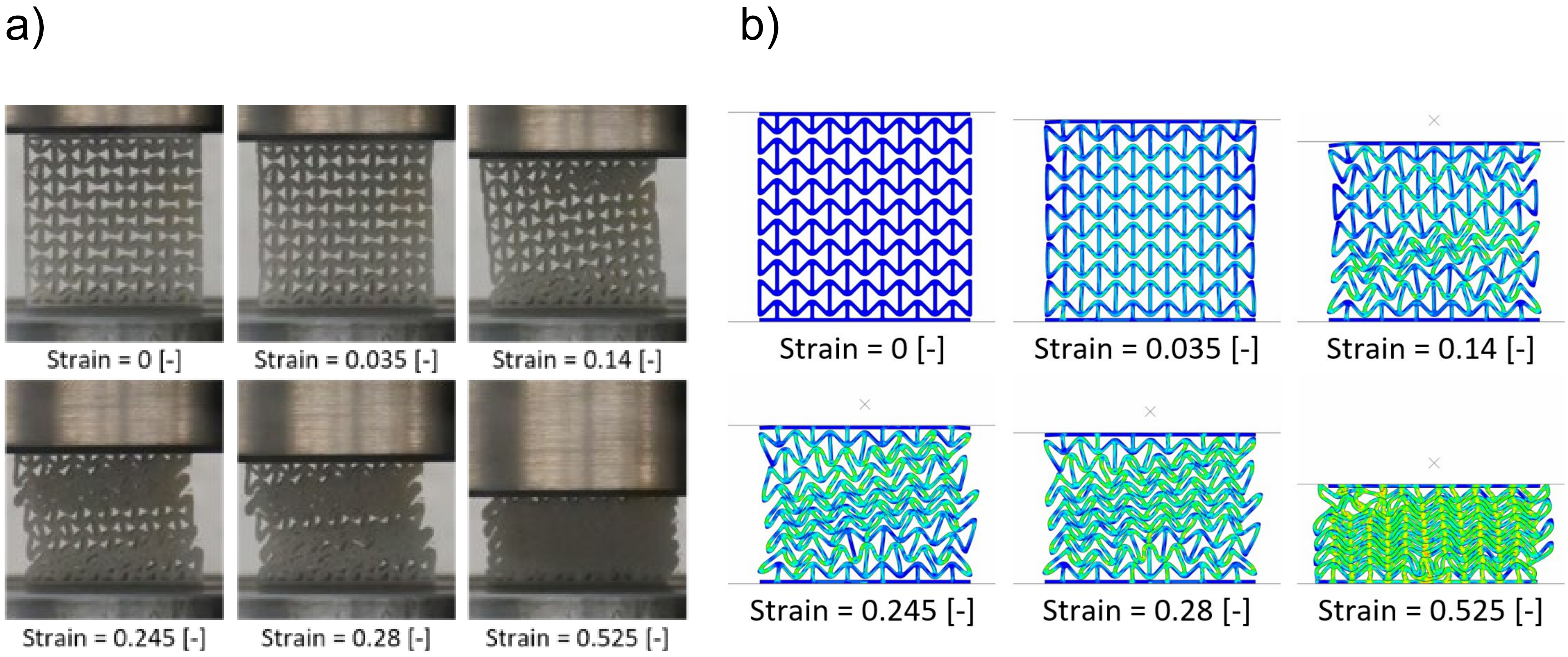
a)
b)
Strain = 0 [-]
Strain = 0.035 [-]
Strain = 0.14 [-]
Strain = 0.245 [-]
Strain = 0.28 [-]
Strain = 0.525 [-]
Strain = 0 [-]
Strain = 0.035 [-]
Strain = 0.14 [-]
Strain = 0.245 [-]
Strain = 0.28 [-]
Strain = 0.525 [-]

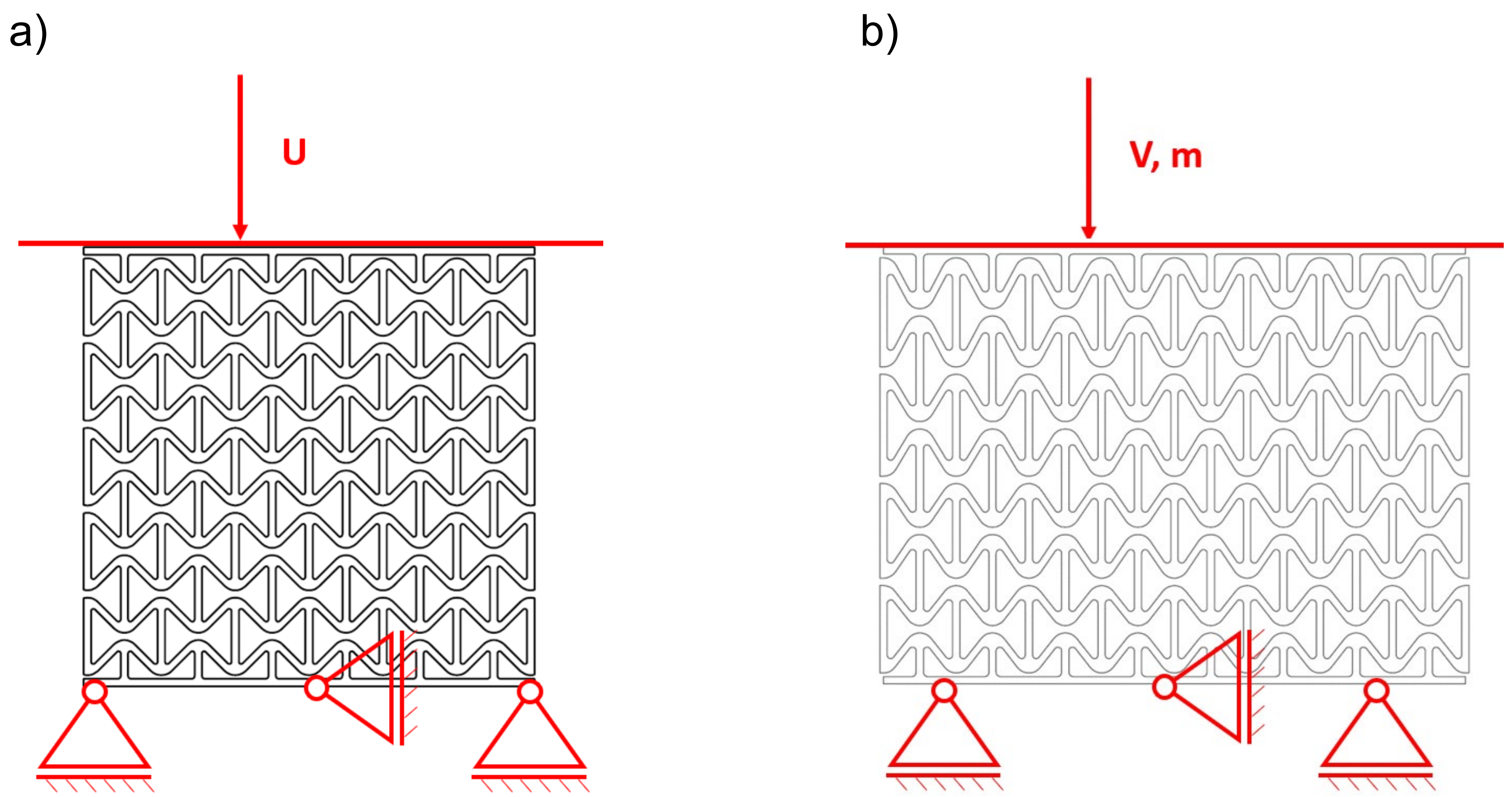

a)
U
b)
V, m

a)

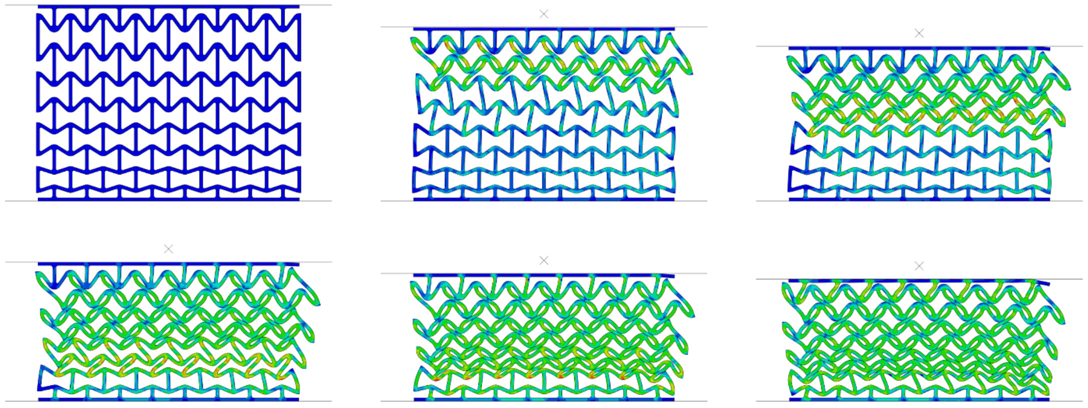

b)

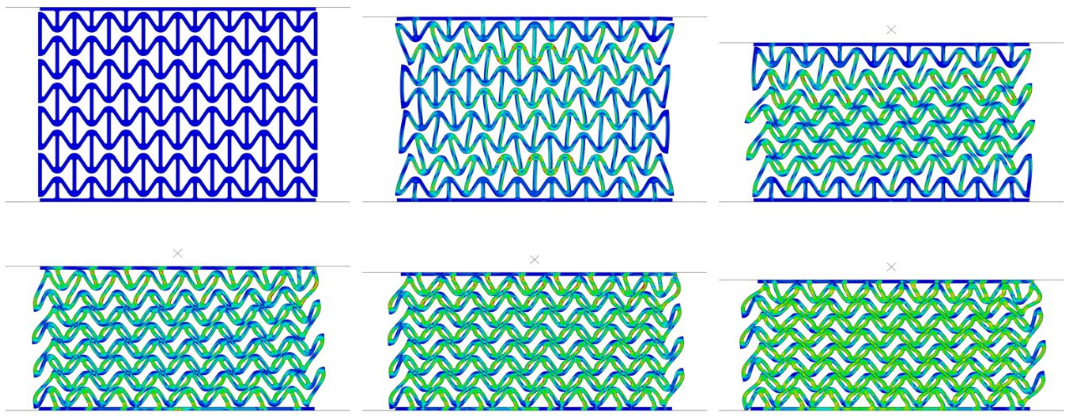

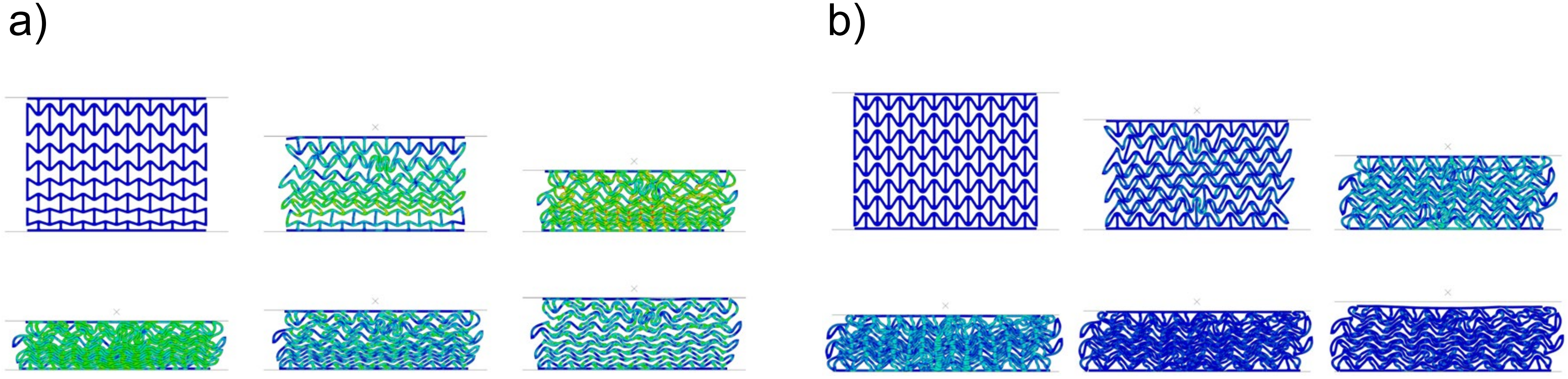
a)
b)